

EEG/MEG Error Bounds for a Static Dipole Source with a Realistic Head Model

Carlos H. Muravchik, *Senior Member, IEEE*, and Arye Nehorai, *Fellow, IEEE*

Abstract—We derive Cramér–Rao bounds (CRBs) on the errors of estimating the parameters (location and moment) of a static current dipole source using data from electro-encephalography (EEG), magneto-encephalography (MEG), or the combined EEG/MEG modality. We use a realistic head model based on knowledge of surfaces separating tissues of different conductivities obtained from magnetic resonance (MR) or computer tomography (CT) imaging systems. The electric potentials and magnetic field components at the respective sensors are functions of the source parameters through integral equations. These potentials and field are formulated for solving them by the boundary or the finite element method (BEM or FEM) with a weighted residuals technique. We present a unified framework for the measurements computed by these methods that enables the derivation of the bounds. The resulting bounds may be used, for instance, to choose the best configuration of the sensors for a given patient and region of expected source location. Numerical results are used to demonstrate an application for showing expected accuracies in estimating the source parameters as a function of its position in the brain, based on real EEG/MEG system and MR or CT images.

I. INTRODUCTION

NEURAL activity in a brain tissue produces an electromagnetic field distribution that can be detected by measuring the induced electric potential or magnetic field. Electro-encephalography (EEG) and magneto-encephalography (MEG) are noninvasive methods for studying the brain activity based on records of electric potentials and magnetic fields. They are used for estimating an instantaneous current distribution representing electrically active tissues with a time resolution on the order of milliseconds. The source of activity is typically described with a model whose parameters are to be estimated.

EEG instruments measure the electric potential at multiple points on the scalp by means of a sensor cap, often with more than hundred electrodes. Available MEG instruments measure the magnetic field, and possibly some of its gradient components, from an array of superconducting quantum interference

device (SQUID) sensors located on a helmet surrounding the head. Modern MEG equipments provide nearly 200 of measurement and the capability of simultaneous EEG recording, with a total of more than 300 sensors for the EEG/MEG combined modality [5], [37].

Evaluation of existing systems and their configuration requires analysis of performance measures. Some of these measures include sensitivity, detectability, capability for resolving (separating) sources, and accuracy in estimating the source parameters. The most common measure of the latter is the mean-square error. In this paper, we compute the Cramér–Rao bound (CRB), rather than concentrating on the mean-square error of a specific algorithm. The CRB provides a lower bound on the variance of the errors in unbiased parameter estimation with the important features of being *universal*, i.e., independent of the algorithm used for estimation among the unbiased ones, and *asymptotically tight*, meaning that for certain distributions, there exist algorithms that achieve the bound as the number of samples becomes large. The CRB is a performance measure that may be useful to do the following.

- 1) Evaluate the efficacy of estimation algorithms.
- 2) Determine regions where good and poor estimation is expected.
- 3) Optimize sensor system design.

In general, a source of cerebral activity is known to act as a current distribution. Current dipoles are the most common model for brain activity partly due to the small number of parameters required for their representation and because they are a good approximation for some real cases [7]. The tissue layers (scalp, skull, cerebro-spinal fluid, brain) enclosing the source are conductive; hence, secondary or volumetric currents induced by the dipole source also circulate. Both types of currents produce an electric potential and magnetic field distribution related to the measurements as expressed through appropriate integral equations [17]. The solution of these equations is a function of the dipole parameters, and this is employed to solve the inverse problem, i.e., finding the source parameters given the measurements.

An important area of EEG/MEG research is devoted to developing realistic head models reducing the set of modeling assumptions. We use a realistic head model based on knowledge of the surfaces separating tissues of different conductivity and the conductivity values of the layers. The surfaces are obtained from images of head cross-sections from magnetic resonance (MR) or computerized tomography (CT) imaging systems. The head cross-sections also enable to obtain a good representation of the surfaces or layers by means of a mesh of small surface or volume elements. We discretize the integral equations for the

Manuscript received May 19, 1999; revised November 6, 2000. This work was supported by the Air Force Office of Scientific Research under Grants F49620-97-1-0481 and F49620-99-1-0067, the National Science Foundation under Grant MIP-9615590, and the Office of Naval Research under Grant N00014-98-1-0542. C. H. Muravchik was also supported by CONICET, Comisión de Investigaciones Científicas de la Pcia. de Buenos Aires (CICPBA), and the Universidad Nacional de La Plata. The associate editor coordinating the review of this paper and approving it for publication was Dr. Joseph M. Francos.

C. H. Muravchik is with the Laboratorio de Electronica Industrial Control e Instrumentacion, Departamento Electrotecnia, Facultad de Ingeniería, University Nacional de La Plata, La Plata, Argentina (e-mail: carlosm@ing.unlp.edu.ar).

A. Nehorai is with the Department of Electrical Engineering and Computer Science, University of Illinois at Chicago, Chicago, IL 60607-7053 USA (e-mail: nehorai@eecs.uic.edu).

Publisher Item Identifier S 1053-587X(01)01423-4.

fields by applying the boundary element method (BEM) [2] or the finite element method (FEM) [19] and solve them with the above representation in small elements of surface or volume, respectively, using a weighted residuals technique. We use a unifying view of these methods to obtain an explicit expression relating the magnetic field at the MEG sensors and electric potential at the EEG sensors to the source parameters. This view and expressions become crucial when we derive the CRB with a realistic head model, as explained below.

Locating current sources inside the skull from EEG or MEG data is more easily approached when the effect of inhomogeneities is fully or partially neglected (layered spherical models are common examples) at the expense of decreased performance. Many important results on performance measures for spherical head models were presented in [10], [11], [20], [28], [30], and [38]. A recent review of the accuracy aspects of estimating dipole parameters has been presented in [47]. Error bounds have been derived using an approximate model that represents the head as spherical layers of different known conductivities as in [31], assuming scalar magnetic sensors, and [18] for scalar or vector magnetic sensors. A spherically symmetric head with scalar magnetic sensors and random conductivities is assumed in [41] using a Bayesian approach. In [33], we introduced the basic ideas to derive the CRB for a realistic head model with possibly vector magnetic sensors. Based on these results, we derive the CRB for the estimation problem with a single snapshot, assuming vector or scalar magnetic sensors, known conductivities and a given mesh. We also compute the bounds for EEG and MEG arrays separately as well as for a combined EEG/MEG array. We consider a single snapshot, implicitly assuming a static source, to avoid complicating the analysis with time evolution issues. In [36], we presented some results considering a propagating dipole source.

Our results can be used for the three general applications of performance bounds mentioned above. For example, they are useful for designing an EEG/MEG study on a patient whose MR or CT information is available. Among other aspects to be resolved before actually performing the EEG/MEG measurements, the position of the EEG electrodes must be chosen. Our CRB can be used to compare various electrode configurations and choose the one that gives the maximum accuracy for a set of plausible dipole positions in the brain that are compatible with the purpose of the study (for instance, somatosensory cortex, temporal lobe, etc.) Computation and analysis time fit perfectly well within the time framework of this sort of study.

More generally, our procedure can be used to compute estimation error bounds for a wide class of inverse problems, whose models are based on partial differential equations [22]. This kind of system arises in many biomedical applications like electro- and magnetocardiography, as well as in chemical substance disposing, nondestructive testing, vapors detection, seismology, magneto-tellurics, or in two-dimensional (2-D) or three-dimensional (3-D) geological and oil prospecting [3], [24], [42].

This paper is organized as follows. In Section II, we review our modeling assumptions for the source, head, noise, and measurements. In Section III, we derive the estimation bounds, and

in Section IV, we give numerical examples for real head and real EEG/MEG systems. In Section V, we discuss the results, limitations, and further work.

II. MEASUREMENT MODELS

Derivation of the CRB requires a functional relationship between the cerebral source and the sensor measurements, as obtained by solving for the distributions of the magnetic field and electric potentials given a source configuration. This implies solving Maxwell's equations for the physical model of source, realistic head and measurements, with the associated boundary values. There is no known closed-form analytic solution to this problem, as in many other similar problems involving PDE with realistic geometry. Alternatively, in [33], we proposed using the expressions obtained by numerical methods employed to solve the *forward problem*, for example, BEM or FEM. Our rationale is that these methods are known to converge to the true solution under certain hypotheses when the mesh or tessellation is sufficiently refined. We will review our assumptions with respect to the physical models for the cerebral source, realistic head, and sensor system configuration before using BEM (or FEM) formulas to establish the required expressions for the measurements.

A. Cerebral Current-Source Model

In general, the current distributions describing sources of neural activity are quite intricate. A common simplifying assumption is to consider a current dipole as a source. This model, which is known as the *equivalent current dipole*, has been shown to accurately depict sources not too deep inside the brain [17] and to permit the associated estimation and accuracy analysis to be carried out fairly simply. More complicated shapes may be approximated by multiple dipoles or multipolar expansions. For simplicity, in this work, we consider only a single dipole of current density

$$\mathbf{J}^p(\mathbf{r}) = \mathbf{q} \cdot \delta(\mathbf{r} - \mathbf{p}). \quad (2.1)$$

The superindex indicates that it is a primary (or impressed) current density, \mathbf{p} is the dipole location, and \mathbf{q} is the dipole moment that determines the intensity and orientation of the dipole.

Denote by $\boldsymbol{\vartheta} = [\mathbf{q}^T, \mathbf{p}^T]^T$ the vector containing the Cartesian coordinates of \mathbf{p} and \mathbf{q} , i.e., the six independent source parameters to be estimated from the measurements. A source modeled by multiple dipoles will need more parameters to be estimated, but $\boldsymbol{\vartheta}$ can be easily extended to that case.

B. Realistic Head Model

From the anatomical point of view, it is possible to consider the head as a number of enclosed volumes made of different tissues whose relevant modeling properties are their geometric configurations and conductivities. We adopt a realistic non-spherical model of the head that considers it to be a volume V of M layers of homogeneous and isotropic volume conductors separated by closed surfaces S_k , $k = 1, \dots, M$ —associated with the scalp, skull, cerebro-spinal fluid, gray, and white matter in the brain—and immersed in an infinite homogeneous

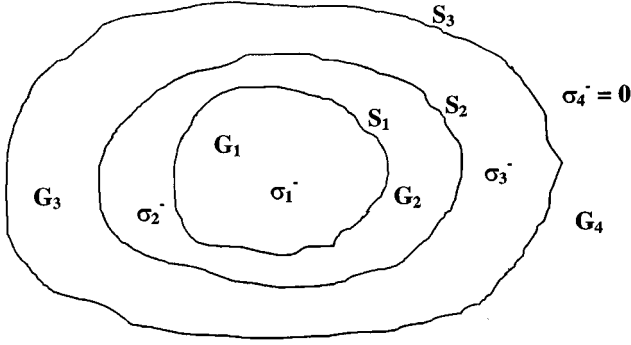


Fig. 1. Sketch of head model with three isotropic conductivity layers.

layer of zero conductivity. Denote by σ_k^- and σ_k^+ the conductivities of the layer inside and outside S_k , respectively. Clearly, $\sigma_k^+ = \sigma_{k+1}^-$; see Fig. 1 for $M = 3$. The geometrical description of the surfaces, i.e., their shapes and positions, is usually based on processing cross-sections of the head obtained by other noninvasive techniques, such as X-ray computed tomography (CT) or magnetic resonance imaging (MRI) [6].

The model also requires knowledge of the layer conductivities, which are known to vary among individuals. Moreover, different researchers have found a large variation on these values [27], even anisotropies in the layers [44]. We will assume the average values for the conductivities given in [14]; these values are commonly used in the field. It is possible to handle anisotropic conductivities using the FEM expressions [50]. Unknown conductivities can be considered as random parameters, originating the approach of [41] to compute the estimation accuracy bound for the spherical head model using Bayesian methods.

C. Sensors and Measurements Model

In EEG, electric potentials at multiple locations on the scalp are typically measured using a cap containing suitable electrodes. An MEG sensor system consists of a helmet with an array of SQUIDs and pick-up coils to measure components associated with the magnetic field \mathbf{B} outside the head. For the combined modality, we assume that the measurement admits the simultaneous recording from the EEG cap and the MEG system. Most modern instruments, for instance, [5] and [37], offer a combination of joint MEG and EEG channels.

Assuming the EEG cap has m_E electrodes, and denoting by $\phi(\mathbf{r}_i)$ the potential at a location \mathbf{r}_i , $i = 1, \dots, m_E$ on the scalp, the vector of potential measurements is

$$\mathbf{y}_E \triangleq \mathbf{v} + \mathbf{e}_E = [\phi(\mathbf{r}_1), \phi(\mathbf{r}_2), \dots, \phi(\mathbf{r}_{m_E})]^T + \mathbf{e}_E \quad (2.2)$$

where \mathbf{e}_E represents the electric noise and modeling errors. Note that for notational convenience, we omit the dependence of $\phi(\mathbf{r}_i)$ on the source parameters $\boldsymbol{\vartheta}$.

The MEG sensor system is very often implemented using pick-up coils in a gradiometric configuration that helps in rejecting some spatial ambient noise. In general, it measures selected components of \mathbf{B} , with the coils acting as magnetometers, and of its gradient tensor $\nabla \mathbf{B}$ for coils in a gradiometric configuration. This kind of sensor is also referred to in the literature as a “vector sensor” [18], [51]. The traditional approach is

to measure just the radial component of the magnetic field, but there are advantages in using other components; see [1]. There are a number of systems that use vector sensors, either existing or under development, such as [37], [46], [48], and [52]. The model of a vector-sensor array is also useful for optimum design and tradeoff between performance and number of channels. The performance of arrays consisting of complete multicomponent sensors (all 12 field and gradient components) at each point is of interest as a benchmark for “best” performance.

Let m_B be the total number of measured components of the magnetic field and its gradient tensor and m_L be the number of measurement locations. Denote by G_r a rectangular matrix that selects and combines these components. Then, the vector of MEG measurements at a point \mathbf{r}_i is given by

$$\begin{aligned} \mathbf{y}_B(\mathbf{r}_i) &= G_{r_i} [\mathbf{B}(\mathbf{r}_i)^T, \text{vec} \nabla \mathbf{B}(\mathbf{r}_i)^T]^T + \mathbf{e}_B(\mathbf{r}_i) \\ &\triangleq \mathbf{b}(\mathbf{r}_i) + \mathbf{e}_B(\mathbf{r}_i) \end{aligned} \quad (2.3)$$

where \mathbf{e}_B represents the magnetic noise and modeling errors. Note that G_{r_i} does not depend on the sensor locations when the same type of sensor is used all over the array. The vector of measurements with an array of sensors located at the points \mathbf{r}_i , $i = 1, \dots, m_L$ is described by stacking the vectors $\mathbf{y}_B(\mathbf{r}_i)$ as follows:

$$\begin{aligned} \mathbf{y}_B &= [\mathbf{y}_B(\mathbf{r}_1)^T, \dots, \mathbf{y}_B(\mathbf{r}_{m_L})^T]^T \triangleq \mathbf{b} + \mathbf{e}_B \\ &= [\mathbf{b}(\mathbf{r}_1)^T, \dots, \mathbf{b}(\mathbf{r}_{m_L})^T]^T + \mathbf{e}_B. \end{aligned} \quad (2.4)$$

In the next subsection, we develop expressions for the potentials \mathbf{v} in (2.2) and the magnetic field \mathbf{B} in (2.3) and (2.4) with a BEM formulation [2], using ideas surveyed, for example, in [17]. In [35], we provide a unified account of our approach for different BEM and FEM formulations that lead to a linear system of equations similar to the BEM used in this paper.

1) *Forward Problem Formulation:* Let $\phi(\mathbf{r})$ be the electric potential at a point \mathbf{r} on the surface S_k , $k = 1, \dots, M$. In [15], an expression is obtained describing the potential distribution by a boundary integral equation involving the geometry, conductivities, and arbitrary source current density $\mathbf{J}^p(\mathbf{r})$, as follows:

$$\begin{aligned} \frac{(\sigma_k^- + \sigma_k^+)}{2} \phi(\mathbf{r}) &= \phi_0(\mathbf{r}) - \frac{1}{4\pi} \sum_{i=1}^M (\sigma_i^- - \sigma_i^+) \int_{S_i} \phi(\mathbf{r}') \\ &\quad \cdot \frac{(\mathbf{r} - \mathbf{r}')}{\|\mathbf{r} - \mathbf{r}'\|^3} \cdot d\mathbf{S}'_i \end{aligned} \quad (2.5)$$

where $d\mathbf{S}'_i$ is an oriented differential area element at the point \mathbf{r}' on the surface S_i . The term $\phi_0(\mathbf{r})$ represents the electrical potential, assuming the same source but immersed in an infinite homogeneous medium of conductivity $1 \Omega^{-1} \text{m}^{-1}$. For the dipole source of (2.1), this term is given by the volume integral

$$\phi_0(\mathbf{r}) = \frac{1}{4\pi} \int_V \mathbf{J}^p(\mathbf{r}') \cdot \frac{(\mathbf{r} - \mathbf{r}')}{\|\mathbf{r} - \mathbf{r}'\|^3} d^3 r' = \frac{1}{4\pi} \frac{\mathbf{q} \cdot (\mathbf{r} - \mathbf{p})}{\|\mathbf{r} - \mathbf{p}\|^3} \quad (2.6)$$

where $d^3 r'$ represents a differential volume element of V .

The magnetic field $\mathbf{B}(\mathbf{r})$ induced at a point \mathbf{r} exterior to V is obtained in [16] and given by

$$\mathbf{B}(\mathbf{r}) = \mathbf{B}_0(\mathbf{r}) + \frac{\mu_0}{4\pi} \sum_{i=1}^M (\sigma_i^- - \sigma_i^+) \int_{S_i} \phi(\mathbf{r}') \frac{(\mathbf{r} - \mathbf{r}')}{\|\mathbf{r} - \mathbf{r}'\|^3} \times d\mathbf{S}'_i \quad (2.7)$$

where $\mu_0 = 4\pi 10^{-7}$ Henry/m is the vacuum magnetic permeability. The term $\mathbf{B}_0(\mathbf{r})$ represents the magnetic field induced at \mathbf{r} by the current density $\mathbf{J}^p(\cdot)$ when the source is immersed in an infinite homogeneous medium of conductivity $1 \Omega^{-1} \text{ m}^{-1}$. For the dipole source of (2.1), this term is given by

$$\begin{aligned} \mathbf{B}_0(\mathbf{r}) &= \frac{\mu_0}{4\pi} \int_V \mathbf{J}^p(\mathbf{r}') \times \frac{(\mathbf{r} - \mathbf{r}')}{\|\mathbf{r} - \mathbf{r}'\|^3} d^3r' \\ &= \frac{\mu_0}{4\pi} \frac{\mathbf{q} \times (\mathbf{r} - \mathbf{p})}{\|\mathbf{r} - \mathbf{p}\|^3}. \end{aligned} \quad (2.8)$$

Observe that both equations (2.5) and (2.7) have two terms on the right-hand side, but only one of these terms depends on the source, through (2.6) and (2.8), respectively. The remaining terms capture the geometry of the head and its electromagnetic behavior. This separation property becomes significant to obtain a practical expression for the CRB.

The BEM formulation of (2.5) and (2.7) involves the solution of integral equations on the layer's boundaries; FEM formulations lead to volume integral equations.

2) *Discretization*: The solution of the boundary integrals is obtained through approximating the electric potentials by a linear combination of suitable basis functions and partitioning the anatomically shaped layer interfaces into triangular elements of small area or surface *tesselation*. The procedure leads to a finite dimensional linear system of equations where the unknowns are the coefficients of the expansion of the potential in the basis functions.

Electric Potential v: We use the conceptually simple but general method of weighted residuals (see [21]) that distributes the error in satisfying (2.5) over all the surfaces. That is, define the residual

$$\begin{aligned} \text{res}(\mathbf{r}) &\triangleq \frac{(\sigma_k^- + \sigma_k^+)}{2} \phi(\mathbf{r}) + \frac{1}{4\pi} \sum_{i=1}^M (\sigma_i^- - \sigma_i^+) \int_{S_i} \\ &\cdot \phi(\mathbf{r}') \frac{(\mathbf{r} - \mathbf{r}')}{\|\mathbf{r} - \mathbf{r}'\|^3} \cdot d\mathbf{S}'_i - \phi_0(\mathbf{r}) \end{aligned} \quad (2.9)$$

and let $w(\mathbf{r})$ be a spatial weighting function. This residual has to be null over the whole domain $S \triangleq \bigcup_{k=1}^M S_k$ when the potential $\phi(\mathbf{r})$ is the proper solution, that is

$$\int_S \text{res}(\mathbf{r}) w(\mathbf{r}) dS = 0. \quad (2.10)$$

The discretization requires that $\phi(\mathbf{r})$ and $w(\mathbf{r})$ be expanded as a linear combination of appropriate basis functions $\{h_n(\mathbf{r})\}$ and $\{w_n(\mathbf{r})\}$, respectively

$$\phi(\mathbf{r}) = \sum_n \phi_n h_n(\mathbf{r}), \quad w(\mathbf{r}) = \sum_n \beta_n w_n(\mathbf{r}) \quad (2.11)$$

where ϕ_n and β_n are real coefficients. There exist several choices of basis functions that generate different methods,

for instance, the center of gravity [45] used in our simulations. This method uses $w_n(\mathbf{r}) = \delta(\mathbf{r} - \mathbf{r}_j^k)$, where \mathbf{r}_j^k is the center of gravity of Δ_j^k , the j th triangle of the surface S_k , and $h_n(\mathbf{r})$ constant on triangles, i.e., $h_n(\mathbf{r}) \equiv 1$, $\mathbf{r} \in \Delta_j^k$ and $h_n(\mathbf{r}) \equiv 0$, $\mathbf{r} \notin \Delta_j^k$. Linear and quadratic interpolation functions for $h_n(\mathbf{r})$ and $w_n(\mathbf{r})$ are also possible. The so-called Galerkin family of methods assumes $h_n(\mathbf{r}) = w_n(\mathbf{r})$. In general, better approximations are achieved at the expense of a larger computational effort.

To obtain a square linear system of equations for the coefficients $\{\phi_n\}$, we truncate both expansions to have N terms. Denote by Φ the vector of coefficients of the linear combination for the electric potential

$$\Phi \triangleq [\phi_1, \phi_2, \dots, \phi_N]^T. \quad (2.12)$$

Define

$$\langle w_i, \phi_0 \rangle \triangleq \int_S \phi_0(\mathbf{r}) w_i(\mathbf{r}) dS. \quad (2.13)$$

Then, the vector of components of the potential $\phi_0(\mathbf{r})$ along the basis functions is given by

$$\Phi_0 \triangleq [\langle w_1, \phi_0 \rangle, \langle w_2, \phi_0 \rangle, \dots, \langle w_N, \phi_0 \rangle]^T. \quad (2.14)$$

In addition, for $i, j = 1, \dots, N$, define the entries

$$D_{ij} \triangleq \sum_{k=1}^M \frac{(\sigma_k^- + \sigma_k^+)}{2} \int_{S_k} w_i(\mathbf{r}) h_j(\mathbf{r}) dS_k \quad (2.15a)$$

$$H_{ij} \triangleq \frac{1}{4\pi} \sum_{k=1}^M (\sigma_k^- - \sigma_k^+) \int_S w_i(\mathbf{r}) \int_{S_k} h_j(\mathbf{r}') \frac{(\mathbf{r} - \mathbf{r}')}{\|\mathbf{r} - \mathbf{r}'\|^3} \cdot d\mathbf{S}'_k \quad (2.15b)$$

and the matrices

$$D \triangleq [D_{ij}], \quad H \triangleq [H_{ij}]. \quad (2.16)$$

Then, the following $(N \times N)$ linear system of equations is obtained from discretization of (2.5)

$$\Phi_0 = (D + H)\Phi \quad (2.17)$$

where the vector of Φ and (2.11) can be used to get the potential at any point on the surfaces but especially at the points where the EEG sensors are placed. This is the so-called forward relation. Given the dipole parameters, Φ is obtained from Φ_0 and knowledge the geometry of the surfaces.

The electric potential obtained by this procedure is known to be unique up to an additive constant. As a consequence, $D + H$ has to have (theoretically) a zero eigenvalue corresponding to the eigenvector $[1, 1, \dots, 1]^T$. A numerical solution to (2.17) may still be obtained by deflation [26] or using the pseudoinverse $(D + H)^\#$

$$\Phi = (D + H)^\# \Phi_0. \quad (2.18)$$

The potential at a sensor point in the outermost surface of V is given by a selection or an interpolation function based on (2.11).

Then, the vector \mathbf{v} of all the measured potentials by the EEG array is

$$\mathbf{v} = H_E \Phi = H_E (D + H) \# \Phi_0 \quad (2.19)$$

where the entries of H_E are typically functions evaluated at the points where the electrodes are located. The matrix H_E captures much of the information concerning the position of the EEG sensors on the head.

Magnetic Field \mathbf{B} : We obtain the explicit relationship between the source parameters and the magnetic field with a parallel procedure to that used above for the potentials. The discretization process is applied to the magnetic field integral equation (2.7), defining a residual by

$$\begin{aligned} \text{res}(\mathbf{r}) = & \mathbf{B}(\mathbf{r}) - \frac{\mu_0}{4\pi} \sum_{i=1}^M (\sigma_i^- - \sigma_i^+) \int_{S_i} \phi(\mathbf{r}') \frac{(\mathbf{r} - \mathbf{r}')}{\|\mathbf{r} - \mathbf{r}'\|^3} \\ & \times d\mathbf{S}'_i - \mathbf{B}_0(\mathbf{r}). \end{aligned} \quad (2.20)$$

A collocation technique has been the common practice to discretize the magnetic equations. That is, the basis functions for the decomposition of $w(\mathbf{r})$ are chosen to be $w_n(\mathbf{r}) \triangleq \delta(\mathbf{r} - \mathbf{r}_n)$, where \mathbf{r}_n is one of the measurement points of the MEG helmet. Define the (3×1) vector (one for each component of the magnetic field)

$$\mathbf{a}_i(\mathbf{r}_n) \triangleq \sum_{k=1}^M (\sigma_k^- - \sigma_k^+) \int_{S_k} h_i(\mathbf{r}') \frac{(\mathbf{r}_n - \mathbf{r}')}{\|\mathbf{r}_n - \mathbf{r}'\|^3} \times d\mathbf{S}'_k \quad (2.21)$$

and the $(3 \times N)$ matrix

$$A(\mathbf{r}_n) \triangleq \frac{\mu_0}{4\pi} [\mathbf{a}_1(\mathbf{r}_n), \mathbf{a}_2(\mathbf{r}_n), \dots, \mathbf{a}_N(\mathbf{r}_n)]. \quad (2.22)$$

We obtain the discretized forward solution of the magnetic field at the MEG sensor points

$$\mathbf{B}(\mathbf{r}) = \mathbf{B}_0(\mathbf{r}) + A(\mathbf{r}) \Phi = \mathbf{B}_0(\mathbf{r}) + A(\mathbf{r}) (D + H) \# \Phi_0. \quad (2.23)$$

Notice that the source parameters are involved only in the terms $\mathbf{B}_0(\mathbf{r})$ and Φ_0 .

A general expression for \mathbf{b} in (2.4) can be derived from (2.23). If the vector of measurements includes components of the gradient tensor of \mathbf{B} , they have to be computed from (2.23) or from (2.7). These tensor components can be ordered into the measurements vectors in the form required by equation (2.3), as shown in [32]. In general, we obtain an equation of the form

$$\mathbf{b} = \mathbf{b}_0 + H_B (D + H) \# \Phi_0 \quad (2.24)$$

where the structure of H_B depends on the specific form of G_{r_i} .

Consider as an example a traditional MEG helmet with m_B coils at the positions \mathbf{r}_i , measuring $\mathbf{B}(\mathbf{r}_i)$ along the unit directions \mathbf{d}_i , $i = 1, \dots, m_L$. In this case, $m_L = m_B$, $G_{r_i} = [\mathbf{d}_i^T, 0]$, and then

$$b(\mathbf{r}_i) = \mathbf{d}_i^T \cdot \mathbf{B}(\mathbf{r}_i), \quad b_0(\mathbf{r}_i) = \mathbf{d}_i^T \cdot \mathbf{B}_0(\mathbf{r}_i). \quad (2.25)$$

We obtain $H_B \triangleq [(\mathbf{d}_1^T A(\mathbf{r}_1))^T \dots (\mathbf{d}_{m_B}^T A(\mathbf{r}_{m_B}))^T]^T$ to use in (2.24) and (2.4).

III. PERFORMANCE BOUNDS

The Cramér–Rao inequality establishes a lower bound on the variance of any unbiased estimator of a set of parameters [49]. One of the features of the CRB is its independence of the algorithm used for the estimation, establishing a universal performance limit among unbiased estimators. Moreover, the CRB is an asymptotically tight bound under certain hypotheses, i.e., there are cases when the bound is achieved as the number of data samples increases. If, for a certain problem, the maximum likelihood estimator exists, then it will achieve the CRB asymptotically [49].

We will derive the CRB for the problem of estimating the source parameters $\boldsymbol{\vartheta} = [\mathbf{q}^T, \mathbf{p}^T]^T = [\vartheta_1, \dots, \vartheta_6]^T$ as described in Section II-A, assuming perfect prior knowledge of the geometry and conductivities of the layers. The resulting bound is easily extended to the case of multiple dipoles, but for simplicity, we will not pursue it here. Let $\hat{\boldsymbol{\vartheta}}$ denote an unbiased estimator of $\boldsymbol{\vartheta}$ and $J(\boldsymbol{\vartheta})$ (the Fisher information matrix). The Cramér–Rao inequality establishes that

$$E\{(\boldsymbol{\vartheta} - \hat{\boldsymbol{\vartheta}})(\boldsymbol{\vartheta} - \hat{\boldsymbol{\vartheta}})^T\} \geq \text{CRB}(\boldsymbol{\vartheta}) = [J(\boldsymbol{\vartheta})]^{-1}. \quad (3.1)$$

The inequality sign means that the difference between the matrices on the left- and right-hand sides is positive semidefinite. The diagonal elements are particularly useful since they set bounds on the variance of each parameter ϑ_i .

Using the measurement models of Section II-C, the combined EEG/MEG measurements are written as $\mathbf{y} = [\mathbf{y}_B^T, \mathbf{y}_E^T]^T$. With equations (2.19) and (2.24), we obtain

$$\mathbf{y} = \begin{bmatrix} \mathbf{b}_0 \\ 0 \end{bmatrix} + \begin{bmatrix} H_B \\ H_E \end{bmatrix} (D + H) \# \Phi_0 + \begin{bmatrix} \mathbf{e}_B \\ \mathbf{e}_E \end{bmatrix} \triangleq \mathbf{m}(\boldsymbol{\vartheta}) + \mathbf{e}. \quad (3.2)$$

The lower part of (3.2) may be used to describe the measurement for EEG alone and the upper for MEG. Therefore, the analysis of either the EEG or MEG modality alone is easily deduced from our general results for the combined modality.

The noise contaminating the signals poses an additional difficulty to the interpretation of the EEG and MEG data. There are two main noise sources: modeling errors and “proper” noise. Modeling errors account for the fit of the physical model to the data. The predominant “proper” noise sources are due to the sensors and instrument self-noise as well as to the sporadic background brain activity [43].

Let \mathbf{e}_E denote the vector of (total) noise affecting the potential measurements (2.2), and let \mathbf{e}_B be the (total) noise affecting the magnetic field measurements (2.4). As it is widely accepted in practice, we assume that the combined modality noise $\mathbf{e} \triangleq [\mathbf{e}_B^T, \mathbf{e}_E^T]^T$ is zero-mean Gaussian with known covariance

$$R \triangleq E\mathbf{e}\mathbf{e}^T = \begin{bmatrix} R_B & R_{BE} \\ R_{EB} & R_E \end{bmatrix}. \quad (3.3)$$

The matrix R can be obtained from prior empirical studies [4], [13], [23], [29] or from modeling [8], [25]. A diagonal noise covariance matrix is assumed very often, representing noise and modeling errors that are uncorrelated between sensors [17], [31], [41]. Some experimental evidence that the covariance

between the modality components of spontaneous brain noise cannot be assumed to be zero has been presented in [39]. However, for the spherically symmetric model of [8], this covariance is analytically shown to be null. Our use of the full covariance matrix of (3.3) allows us to derive the error bounds for the general case.

With the measurement model (3.2) and the Gaussian noise model, the (i, j) th entry of the Fisher information matrix is [18]

$$J_{ij}(\boldsymbol{\vartheta}) = [\{\text{CRB}(\boldsymbol{\vartheta})\}^{-1}]_{ij} = \frac{\partial \mathbf{m}^T}{\partial \vartheta_i} R^{-1} \frac{\partial \mathbf{m}}{\partial \vartheta_j}. \quad (3.4)$$

With the noise covariance (3.3), we easily obtain from (3.4) that

$$\begin{aligned} J_{ij}(\boldsymbol{\vartheta}) = & \left(\frac{\partial \mathbf{b}_0}{\partial \vartheta_i} \right)^T (R_B - R_{BE} R_E^{-1} R_{EB})^{-1} \frac{\partial \mathbf{b}_0}{\partial \vartheta_j} \\ & + \left(\frac{\partial \Phi_0}{\partial \vartheta_i} \right)^T (D + H)^{\#T} [H_B^T H_E^T] R^{-1} \begin{bmatrix} H_B \\ H_E \end{bmatrix} \\ & \cdot (D + H)^{\#} \frac{\partial \Phi_0}{\partial \vartheta_j} \\ & + 2 \left\{ \left(\frac{\partial \Phi_0}{\partial \vartheta_i} \right)^T (D + H)^{\#T} [H_B^T H_E^T] R^{-1} \right. \\ & \quad \left. \cdot \begin{bmatrix} \frac{\partial \mathbf{b}_0}{\partial \vartheta_j} \\ 0 \end{bmatrix} \right\}_s \end{aligned}$$

where $\{A\}_s \triangleq (A + A^T)/2$. As explained above, when assuming that either

- i) the modeling errors predominate over other sources of noise;
- ii) all the noise components are independent and spatially uncorrelated with the same Gaussian distribution;
- iii) prewhitening was used

then the covariance matrix becomes diagonal

$$R = \mathbf{E} \mathbf{e} \mathbf{e}^T = \begin{bmatrix} \sigma_B^2 I_{m_B} & 0 \\ 0 & \sigma_E^2 I_{m_E} \end{bmatrix} \quad (3.5)$$

which is frequently assumed. For (3.5), the Fisher information matrix specializes to

$$\begin{aligned} J_{ij}(\boldsymbol{\vartheta}) = & \frac{1}{\sigma_B^2} \left(\frac{\partial \mathbf{b}_0}{\partial \vartheta_i} \right)^T \frac{\partial \mathbf{b}_0}{\partial \vartheta_j} \\ & + \left(\frac{\partial \Phi_0}{\partial \vartheta_i} \right)^T (D + H)^{\#T} \left[\frac{H_B^T H_B}{\sigma_B^2} + \frac{H_E^T H_E}{\sigma_E^2} \right] \\ & \cdot (D + H)^{\#} \frac{\partial \Phi_0}{\partial \vartheta_j} \\ & + 2 \left\{ \left(\frac{\partial \Phi_0}{\partial \vartheta_i} \right)^T (D + H)^{\#T} \frac{H_B^T \frac{\partial \mathbf{b}_0}{\partial \vartheta_j}}{\sigma_B^2} \right\}_s. \quad (3.6) \end{aligned}$$

Observe that a large portion of the computational effort to numerically calculate the CRB lies in computing the entries of H_B and $D + H$, perhaps by means of numerical integration and the

pseudoinverse of $D + H$. For a surface tessellation in triangles, there exist analytic formulas that allow rapid and efficient calculation of (2.15a), (2.15b), and (2.21), [9], [12]. The computation of the pseudoinverse is time consuming since the size of the matrices involved is large, depending on the number of elements or nodes used in the tessellation N . In a typical BEM case, if a very precise representation of the surfaces is not needed, the matrix $D + H$ may have a size between (1000×1000) and (2000×2000) , although $N = 10\,000$ is often found. The need for either better precisions or the use of FEM may lead to even larger matrices. However, this is not a problem for calculating the bound since, as we show below, the pseudoinverse needs to be computed only once per sensor configuration and must be patient.

The actual computation of the bound is greatly simplified by the fact that the terms of $\mathbf{m}(\boldsymbol{\vartheta})$ that depend on $\boldsymbol{\vartheta}$, namely, \mathbf{b}_0 and Φ_0 , are well separated from the geometry- and conductivity-dependent matrices H_B , H , D and H_E . Indeed, the partial derivatives in (3.4) only affect the terms \mathbf{b}_0 and Φ_0 . When the CRB has to be calculated for several values of the source parameters, it suffices to compute $(D + H)^{\#}$ only once, regardless of the values of the source parameters. This fact dramatically reduces the amount of computations needed to calculate the bounds.

From (3.5) and (3.6), it is possible to infer how the EEG and MEG add their respective amount of information into the Fisher matrix $J(\boldsymbol{\vartheta})$. Essentially, the ‘‘larger’’ this matrix is, the ‘‘smaller’’ the bound will be. Since, under proper conditions, it is an asymptotically tight bound, there should exist an algorithm that achieves it asymptotically. This means that if, for instance, due to a change in the position of the EEG cap, the matrix H_E changes, causing the CRB to decrease, then a smaller estimation error variance may be obtained.

When the noise components \mathbf{e}_E and \mathbf{e}_B are independent as in (3.6), then the Fisher matrix in the combined modality is the sum of the matrices for EEG and MEG alone, i.e.,

$$\begin{aligned} J_{ij}^{\text{EEG}}(\boldsymbol{\vartheta}) = & \left(\frac{\partial \Phi_0}{\partial \vartheta_i} \right)^T (D + H)^{\#T} \frac{H_E^T H_E}{\sigma_E^2} (D + H)^{\#} \\ & \cdot \frac{\partial \Phi_0}{\partial \vartheta_j}, \quad (3.7a) \end{aligned}$$

$$\begin{aligned} J_{ij}^{\text{MEG}}(\boldsymbol{\vartheta}) = & \frac{1}{\sigma_B^2} \left(\frac{\partial \mathbf{b}_0}{\partial \vartheta_i} \right)^T \frac{\partial \mathbf{b}_0}{\partial \vartheta_j} + \left(\frac{\partial \Phi_0}{\partial \vartheta_i} \right)^T (D + H)^{\#T} \\ & \cdot \frac{H_B^T H_B}{\sigma_B^2} (D + H)^{\#} \frac{\partial \Phi_0}{\partial \vartheta_j} \\ & + 2 \left\{ \left(\frac{\partial \Phi_0}{\partial \vartheta_i} \right)^T (D + H)^{\#T} \frac{H_B^T \frac{\partial \mathbf{b}_0}{\partial \vartheta_j}}{\sigma_B^2} \right\}_s. \quad (3.7b) \end{aligned}$$

However, if the noise components are correlated as in (3.5), there might be an additional contribution to $J^{\text{MEG}} + J^{\text{EEG}}$ due to the combined modality. Depending on the sign of the covariance between \mathbf{e}_E and \mathbf{e}_B , the contribution would be additive or subtractive. The work in [39] seems to suggest that the covariance R_{EB} increases the information and, hence, lowers the CRB of the combined modality.

Remark on Optimization: Assume that knowledge of a patient's internal head surfaces is available and that a certain "wide" region of his head is targeted to be explored with EEG and MEG. The relative position of the EEG cap with respect to the MEG helmet can be chosen to decrease the CRB in the region of interest, potentially improving the equipment configuration to estimate the source parameters. This procedure may be performed before any EEG/MEG measurements are actually taken, and it illustrates one of the practical uses of the CRB.

A. Constrained Bounds: Tangential Dipoles

Previous work on the CRB considered current sources that were either known or assumed to be only tangential dipoles. As explained in Section II-A, this is because radial dipoles are invisible to the MEG sensors under a spherically symmetric head model. In the context of our realistic head model, the concept of radial and tangential dipoles is not very well defined, but it has some interest for comparisons with the CRB for spherical models.

From a *global* point of view, a sphere can be a crude approximation to the shape of the head. Its "center" \mathbf{c} can be computed as the center of mass of the brain surface or, equivalently, the point that minimizes the sum of squared distances to the brain surface. Thus, extrapolating the concept of a tangential direction to a sphere, we define a tangential dipole of moment \mathbf{q} at the position \mathbf{p} as one with $(\mathbf{p} - \mathbf{c}) \perp \mathbf{q}$. The position vector \mathbf{p} measured from \mathbf{c} , which is denoted as $\tilde{\mathbf{p}}$, is given in Cartesian coordinates by

$$\tilde{\mathbf{p}} = \tilde{p}[\sin \theta \cos \varphi, \sin \theta \sin \varphi, \cos \theta]^T \quad (3.8)$$

where

- θ dipole's elevation (measured from the z -axis);
- φ its azimuth (measured from the x -axis);
- \tilde{p} length of $\tilde{\mathbf{p}}$.

The vectors

$$\mathbf{u}_\theta = [\cos \theta \cos \varphi, \cos \theta \sin \varphi, -\sin \theta]^T \quad (3.9a)$$

$$\mathbf{u}_\varphi = [\sin \varphi, \cos \varphi, 0]^T \quad (3.9b)$$

$$\mathbf{u}_{\tilde{p}} = \tilde{\mathbf{p}}/\tilde{p} \quad (3.9c)$$

form an orthonormal basis that allows a simple description of tangential and radial dipoles, which will be considered later.

An alternative way of defining radial and tangential components is using a *local* point of view. A (locally) tangential dipole is one whose \mathbf{q} vector is parallel to a patch of brain surface neighboring the tip of \mathbf{p} . However, this vector only seldom satisfies $\tilde{\mathbf{p}} \perp \mathbf{q}$. Therefore, we adopt the global definition. In local coordinates, at the tip of \mathbf{p} , the dipolar moment of a tangential dipole is of the form $\mathbf{q}_t = q_\theta \mathbf{u}_\theta + q_\varphi \mathbf{u}_\varphi$, whereas a radial one is like $\mathbf{q}_r = q_{\tilde{p}} \mathbf{u}_{\tilde{p}}$. Of course, any dipole may be written as $\mathbf{q} = \mathbf{q}_t + \mathbf{q}_r$.

The orthogonality of the source parameter vector, i.e., $\mathbf{q} \perp (\mathbf{p} - \mathbf{c})$, introduces an additional constraint that has to be incorporated in the CRB formula, as shown in [18]. Equivalently, the amount of information provided by the same measurements when the dipole is in arbitrary position and when it is known to be tangential are different. To deal with tangential dipoles,

we use the orthonormal vector basis introduced in (3.9a), implying that there are only five parameters left to be estimated $\mathbf{cta} = (\theta, \varphi, \psi, p, q)$, with $\tan \psi = -q_\theta/q_\varphi$. Therefore, the CRB has to be modified to account for the change of the vectors \mathbf{q} and \mathbf{p} to the coordinates (3.9a) and to incorporate the constraint $\mathbf{q} \perp (\mathbf{p} - \mathbf{c})$.

Error bounds for this type of orthogonal set of unknown vectors were derived in [18]. Consider the right orthogonal system to be estimated $\{\mathbf{v}_1, \mathbf{v}_2, \mathbf{v}_3\} \triangleq \{\tilde{\mathbf{p}}, \mathbf{q}, (\tilde{\mathbf{p}} \times \mathbf{q})/\|\tilde{\mathbf{p}} \times \mathbf{q}\|\}$ and its orthonormal version $\{\mathbf{u}_1, \mathbf{u}_2, \mathbf{u}_3\}$. Let $\hat{\mathbf{v}}_i$ be an unbiased estimate of \mathbf{v}_i , and define $\delta \mathbf{v}_i \triangleq (\hat{\mathbf{v}}_i - \mathbf{v}_i)$; we are interested in bounding $E\|\delta \mathbf{v}_i\|^2$. Let K be the matrix

$$K \triangleq \begin{bmatrix} \mathbf{u}_1 \cdot \partial \mathbf{v}_1 / \partial \eta_1 & \mathbf{u}_1 \cdot \partial \mathbf{v}_1 / \partial \eta_2 & \cdots & \mathbf{u}_1 \cdot \partial \mathbf{v}_1 / \partial \eta_5 \\ \mathbf{u}_2 \cdot \partial \mathbf{v}_2 / \partial \eta_1 & \mathbf{u}_2 \cdot \partial \mathbf{v}_2 / \partial \eta_2 & \cdots & \cdot \\ \mathbf{u}_3 \cdot \partial \mathbf{v}_3 / \partial \eta_1 & \cdots & \cdots & \\ \mathbf{u}_3 \cdot \partial \mathbf{v}_2 / \partial \eta_1 & \cdots & \cdots & \\ \mathbf{u}_1 \cdot \partial \mathbf{v}_3 / \partial \eta_1 & \cdots & \cdots & \\ \mathbf{u}_2 \cdot \partial \mathbf{v}_1 / \partial \eta_1 & \cdots & \cdots & \end{bmatrix} \quad (3.10)$$

and define

$$C \triangleq K \cdot \text{CRB}(\boldsymbol{\eta}) \cdot K^T. \quad (3.11)$$

Then, it is shown in [18] that

$$E\|\delta \tilde{\mathbf{p}}\|^2 \geq C_{1,1} + \tilde{p}^2 C_{5,5} + C_{6,6} \quad (3.12a)$$

$$E\|\delta \mathbf{q}\|^2 \geq C_{2,2} + (q/\tilde{p})^2 C_{6,6} + C_{4,4} \quad (3.12b)$$

where $C_{i,i}$ are the diagonal entries of C . An interesting feature of (3.12a) is that the contribution to the position error bound can be split into a longitudinal component of the error along $\tilde{\mathbf{p}}$ and a lateral component that is orthogonal to $\tilde{\mathbf{p}}$. Indeed, the longitudinal component of the error bound is given by the first term on the right-hand side and the lateral by the sum of the second and third terms of (3.12a). Similarly, from (3.12b), the error bound for the dipole moment \mathbf{q} can be split into a longitudinal component, which is given by the first term on the right-hand side, and a lateral, which is given by the sum of the second and third terms.

The partial derivatives in K can be routinely calculated and do not involve information from the tessellation or conductivities. Observe that (3.11) requires $\text{CRB}(\boldsymbol{\eta})$. However, it is sometimes less tedious to compute the CRB using the parameters $\boldsymbol{\vartheta}$ rather than $\boldsymbol{\eta}$. Therefore, we have to transform from variables $\boldsymbol{\eta}$ to $\boldsymbol{\vartheta}$. A well-known formula [40] gives $\text{CRB}(\boldsymbol{\eta}) = T \cdot \text{CRB}(\boldsymbol{\vartheta}) \cdot T^T$, where $T \triangleq \partial \boldsymbol{\eta} / \partial \boldsymbol{\vartheta}$ is the Jacobian matrix of the transformation. This results in the expression $C \triangleq \overline{K} \cdot \text{CRB}(\boldsymbol{\vartheta}) \cdot \overline{K}^T$, with $\overline{K} = KT$, as we presented in [34].

IV. NUMERICAL EXAMPLES

The CRB results can be used in several ways. For instance, when a number of candidate source locations and moments is available and there is a need to assess the accuracy that a sensors' configuration is able to achieve, before any EEG or MEG measurement is taken on the patient, changes in the number of

sensors, especially the number of electrodes of the EEG cap and their locations, can be made to explore the most advantageous configuration to perform the actual measurement.

In the examples below, we are mostly concerned with the way the CRB results are presented. We focus on location estimates, but similar techniques can be used to analyze the dipole moment error.

We have conducted numerical examples to determine the error bounds as a function of the dipole position and (globally tangential) moment. Tangential dipoles have been chosen in order to facilitate comparisons with bounds computed for spherical models of the head. However, recalling the discussion of Section III-A, these dipole moments have a component that is parallel to the local surface as well as a radial one whose relative size depends on the dipole location.

We use three kinds of representation of the results.

- 1) With dipole locations on the (x, z) sagittal plane, we obtain equal precision contours.
- 2) With dipole sources on a spherical surface, we show the error bounds as a tone of a gray (or color) scale for each dipole location.
- 3) For dipoles located on a spherical surface, we depict the volume of the ellipsoid of 90% probability of finding the dipole inside as a tone of a gray scale.

In all the examples, the bounds were calculated for a given tessellated real head, with three layers of 652 triangles per surface. The conductivity values were assumed to be $0.33 \Omega^{-1} \text{m}^{-1}$ for the scalp and brain and $0.0042 \Omega^{-1} \text{m}^{-1}$ for the skull, as given in [14].

The sensors configuration consisted of an MEG whole head helmet and an EEG cap. The reference coordinates frame was placed at the pole of the MEG helmet, with the positive x -axis pointing to the front, the positive y -axis to the left side, and the negative z -axis into the head. The helmet was symmetrically centered and placed at a distance of about 2 cm above the head. It was the same as the one used in [20] by BTi researchers, consisting of 160 magnetometer coils configured in rings on a spherical surface. The coil axes have pick-up directions \mathbf{d}_i and are not all radially oriented, therefore corresponding to the magnetic field measurement model of (2.4), (2.24), and (2.25).

The EEG cap had 37 electrodes as in [31] in rings of one, six, 12, and 18 electrodes. The rings are equally spaced and cover an elevation angle of 30° . The electrodes in a ring are also equally spaced. The pole of the cap, where only one sensor sits, was placed on the scalp below the pole of the MEG helmet.

In Fig. 2, we show a cross-section of the sensors' locations and the scalp in the (x, z) -plane. The EEG electrodes that lie in this plane are shown as asterisks (*). The locations of the magnetometer coils of the MEG helmet in the (x, z) -plane are displayed with (\circ). Each coil location is shown with an arrow that points along the unit vector $-\mathbf{d}_i$, i.e., opposite from the pick-up direction. The nodes of the scalp tessellation that lie in the (x, z) plane are shown with (\bullet). For clarity, we also include a cross-section of the scalp obtained by cubic 2-D interpolation of the scalp tessellation nodes.

The source and noise were chosen as in [31] or [41] to facilitate comparisons, i.e., $q = 10 \text{ nAm}$ and $\sigma_B = 35 \text{ fT}$, $\sigma_E = 0.4 \mu\text{V}$.

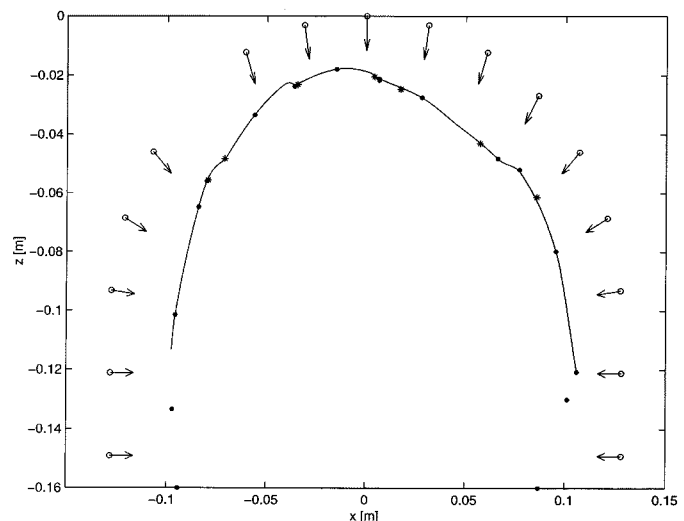


Fig. 2. MEG (\circ) and EEG ($*$) sensors on the (x, z) plane and the MEG pick-up directions. Tessellation nodes (\bullet) on the (x, z) plane of the scalp and the 2-D cubic interpolation cross-section in continuous line are also shown.

With regard to the discretization technique for the electric potentials, we chose a simple “center of gravity” method. Denote by Δ_j^k the j th triangle of the k th surface S_k and by \mathbf{r}_j^k the center of gravity of Δ_j^k . The technique consists of i) collocation at the centers of gravity of the tessellation triangles, i.e., $\psi_j^k(\mathbf{r}) = \delta(\mathbf{r} - \mathbf{r}_j^k)$ and ii) a subdomain method that assumes constant potentials on the triangles, i.e.,

$$\varphi_i^j(\mathbf{r}) = \begin{cases} 1, & \text{if } \mathbf{r} \in \Delta_j^i \\ 0, & \text{otherwise.} \end{cases} \quad (4.1)$$

The magnetic field was discretized as explained in Section II-C2.

A. Contours of Equal Error Bound

We computed the unconstrained position error bounds for dipoles located on a uniform grid with a step of 5 mm on the (x, z) -plane within the brain surface. Dipole moment orientations were (globally) tangential with 12 equally spaced values of ψ at each location. The bounds for the different tangential orientations were averaged to present one error bound value per dipole location. The results are presented as contours with the same averaged position error. That is, a contour line joins all the dipole locations having the same level of expected accuracy.

Figs. 3–5 show the position error bounds in meters for EEG alone, MEG alone, and the EEG/MEG combination. The bounds presented in these figures use the unconstrained CRB of (3.7a) and (3.7b). Note that a direct comparison between EEG and MEG is unfair since the number of sensors and the area covered by each array is quite different. However, what can be easily seen is the gain due to the combined modality. Indeed, it is possible to estimate deeper dipoles with a significantly better accuracy using the combined modality rather than using any of the single modalities. The level curves also suggest that a plausible scalar measure of comparison among alternative configurations is the volume between a surface of constant accuracy level and

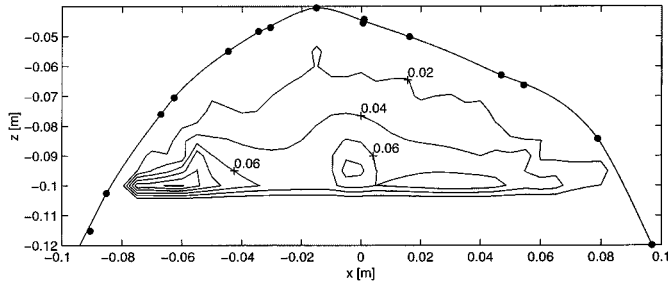


Fig. 3. EEG contours of equal position error bounds in meters for tangential dipoles in the (x, z) plane.

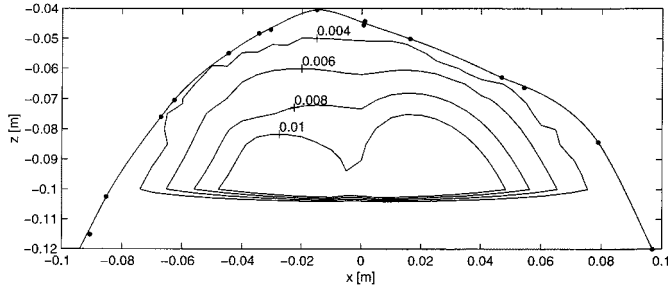


Fig. 4. MEG contours of equal position error bounds in meters for tangential dipoles in the (x, z) plane.

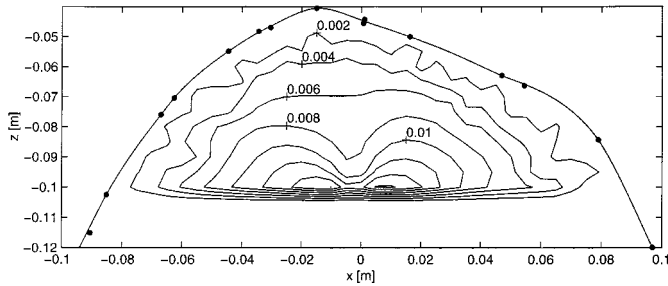


Fig. 5. EEG/MEG contours of equal position error bounds in meters for tangential dipoles in the (x, z) plane.

the brain, which is an idea close to the *half sensitivity volume* suggested in [27].

The asymmetry between the head front ($x > 0$) and back ($x < 0$) in Fig. 3 is due to the shape asymmetry of the conducting volume and the relatively small area covered by the EEG cap; see also Fig. 2. The accuracy in the MEG case in Fig. 4 is seen to be especially better for dipoles that are closer to the brain surface. When considering deeper dipoles, the accuracy worsens, as expected, due to the increased distance to the sensors. The dip in the center is roughly explained because the accuracy in the front or the back part of the figure is dominated by the closest MEG sensors, whereas the dipoles in the center are equally far from all the helmet sensors. In addition, notice that the MEG helmet is centered at $x = y = z = 0$, which is located somewhat further from the front part of the brain surface; see Fig. 2. This causes the front lobe of the contour for 0.01 cm to be somewhat higher than the back lobe. This effect is compensated in the combined modality by the opposite behavior of EEG, as can be seen in Fig. 5. From this figure, we infer that the dipole positions can be estimated with less than 2 mm error bound in a strip of more than 1 cm of depth in the brain (gray

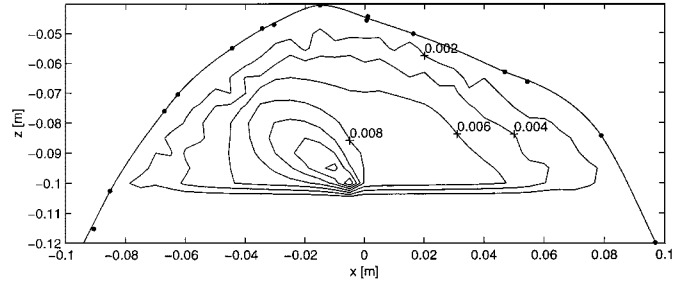


Fig. 6. EEG/MEG contours of equal depth (longitudinal) position error.

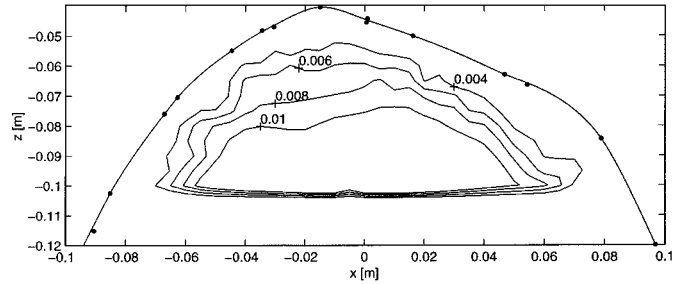


Fig. 7. EEG/MEG contours of equal lateral position error.

matter), below the region covered by the MEG helmet. This strip is deeper in the upper part of the brain, below the EEG cap.

Figs. 6 and 7 show separately the error bounds of the depth (longitudinal) and lateral components of the position error for the combined EEG/MEG, using the constrained bound of (3.1). It is interesting to note that for curves of the same level, the estimation of the depth component outperforms the lateral component. This is true especially for deeper dipoles. In other words, the depth of the source can be better estimated than its position sideways and that this effect is more noticeable for deeper brain regions.

B. Surface of Error Bound

In the previous example, we displayed results from dipoles on a cross-section plane of the head. In order to show information from sources in the whole head, we consider tangential dipole sources lying on a spherical surface within the brain. The center c of the sphere was chosen to be the point that minimizes the squared distance to the nodes of the tessellation of the brain surface. We computed the error bound for each source location on the sphere surface and depicted it in a gray scale. As we discussed in Section III-A, if a local definition of tangential dipoles were required, like being parallel to the brain surface in a certain region, a spherical surface could be fitted to that region and the dipoles placed tangentially on it.

In Figs. 8–10, the dipoles lie on a sphere that is 55 mm in diameter, which is about 30 mm below the upper part of the brain surface; thus, it depicts rather deep dipoles. It turns out that this sphere intersects the brain surface in its lower part where there is not much neuronal activity of interest (brainstem is a notable exception); therefore, only the results for the part of the sphere inside the brain are shown. Moreover, we present only the points where the position error bound is better than 10 mm since the distribution of larger errors is of no practical interest. The figures

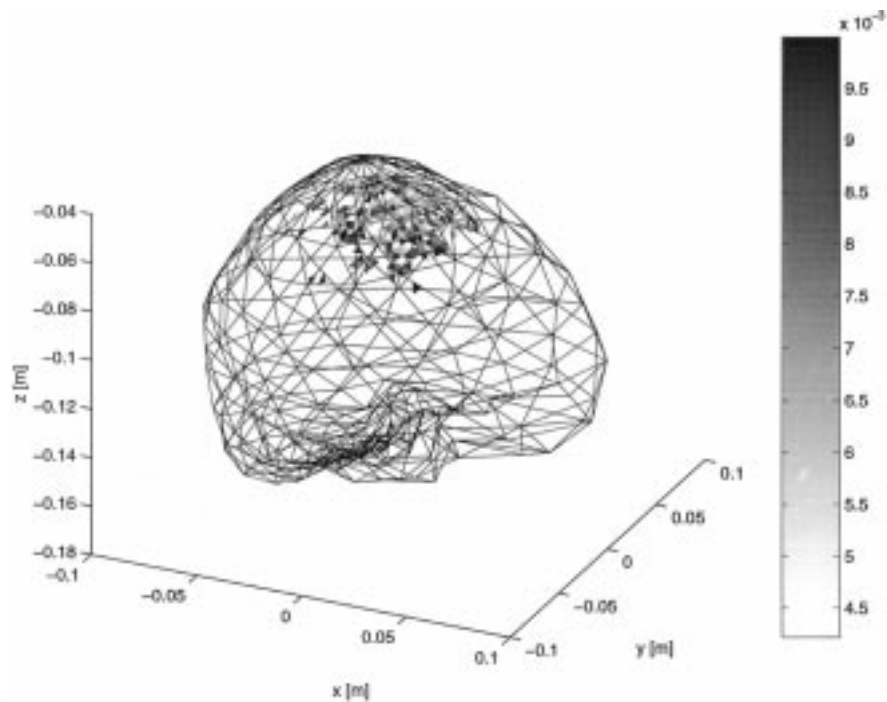


Fig. 8. Error bounds of EEG for tangential dipoles on a sphere. Only dipoles inside the brain and with bounds less than 10 mm are shown.

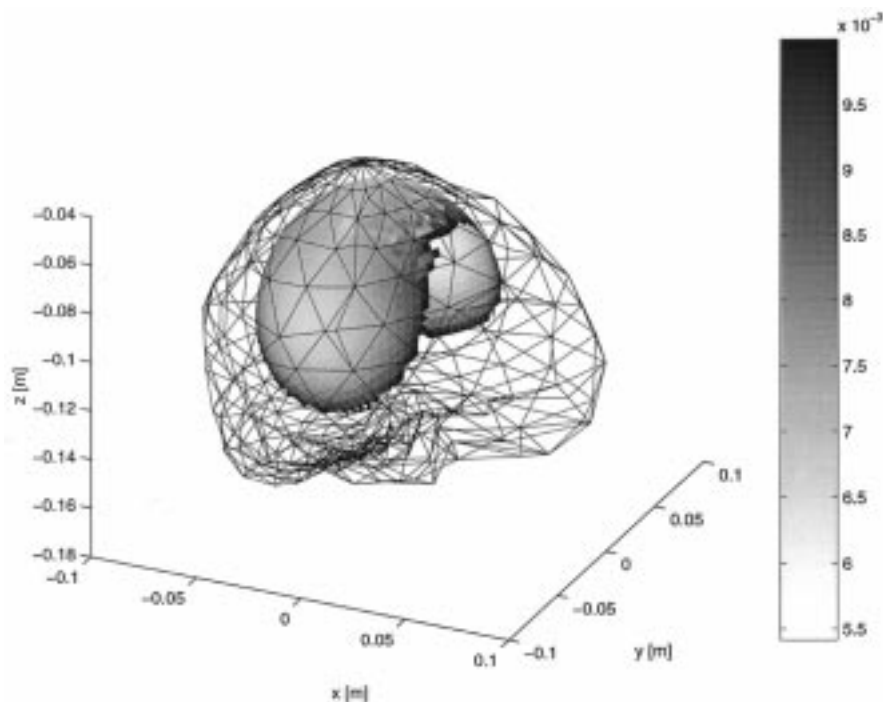


Fig. 9. Error bounds of MEG for tangential dipoles on a sphere. Only dipoles inside the brain and with bounds less than 10 mm are shown.

also show the tessellated brain surface as if it was transparent in order to provide a space reference.

In Fig. 8, it can be seen that the region of better accuracy is below the EEG cap toward the front part ($x > 0$), where the cap is closer to the sphere. Fig. 9 shows results for the MEG helmet, and here, the region of better accuracy spreads over a larger area than with EEG. This could be attributed to the larger area covered by the helmet with magnetic sensors than with the cap. It can be seen that on the top and on the temporal lobes (both

sides), the accuracy is better and worsens toward the back or the front lobe. This is due to the spherical surface that is deeper in the back or the front than in the sides or the top of the head. This sort of effect is avoided if the bound was analyzed for dipoles on a local sphere; for instance, fitting the right temporal lobe.

In Fig. 10, for EEG/MEG, we see that the area of better accuracy is wider than in Figs. 8 or 9. Moreover, it also achieves lower bounds than EEG or MEG at each location. This again motivates, as expected, the use of the combined modality.

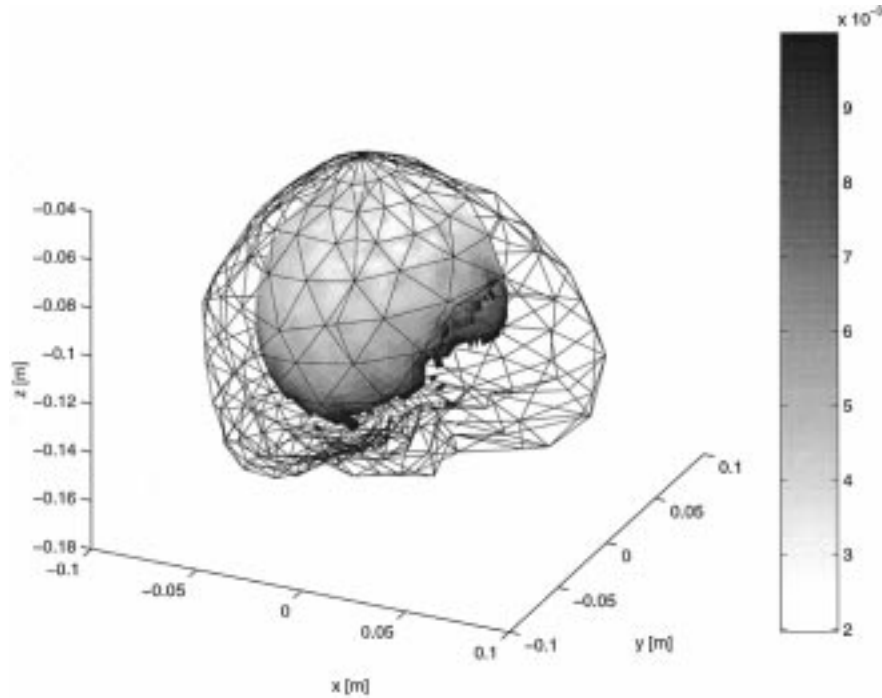


Fig. 10. Error bounds of EEG/MEG for tangential dipoles on a sphere. Only dipoles inside the brain and with bounds less than 10 mm are shown.

C. Surface of Volume of 90% Confidence

It is not possible in a single 3-D figure to condensely display the head geometry and the error bounds for all the parameters. A useful scalar measure of estimation accuracy is the volume of the 90% probability concentration ellipsoid [47]. That is, for each dipole location, the CRB gives us a bound on the error covariance matrix of the dipole position vector. On the other hand, the volume of the 90% probability concentration ellipsoid is the volume of the ellipsoid that encloses the mean of an unbiased estimate with 90% probability. With the CRB, we can approximate that volume, as shown below.

Let $\bar{\mathbf{p}} = \hat{\mathbf{p}} - \mathbf{p}$ be the position error vector when estimating \mathbf{p} with $\hat{\mathbf{p}}$, and let $R = E\{\bar{\mathbf{p}}\bar{\mathbf{p}}^T\}$ be its covariance matrix. An ellipsoid in $\bar{\mathbf{p}}$ -space is defined by

$$c^2 = \bar{\mathbf{p}}^T R^{-1} \bar{\mathbf{p}} \leq \bar{\mathbf{p}}^T \text{CRB}^{-1} \bar{\mathbf{p}}. \quad (4.2)$$

The constant c is to be determined for the ellipsoid to have 90% probability of enclosing the tip of the true dipole position vector \mathbf{p} . Indeed, under a Gaussian hypothesis and an n -dimensional error vector, c must satisfy [49]

$$1 - 0.90 = \frac{n}{2^{n/2}\Gamma(n/2 + 1)} \int_c^\infty \lambda^{n-1} \exp^{-\lambda^2/2} d\lambda \quad (4.3)$$

where $\Gamma(\cdot)$ denotes the gamma function. The volume of the 90% concentration ellipsoid is given by

$$\mathcal{V} = \frac{\pi^{n/2} c^n |R|^{1/2}}{\Gamma(n/2 + 1)}. \quad (4.4)$$

When the distribution of $\bar{\mathbf{p}}$ is not Gaussian, c calculated with (4.3) is only an approximation to the true value, and the ellipsoid

of (4.2) encloses the tip of \mathbf{p} with a probability other than 90%. We will use the constrained $|\text{CRB}|$ rather than $|R|$. However, the volume of the ellipsoid \mathcal{V} still remains a valid tool to represent the concept of concentration of estimates around the true value.

Therefore, we propose to use the volume \mathcal{V} to have an overall picture of the achievable accuracy at each dipole location. We examine the accuracy for dipoles on the same spherical surfaces as in the previous example. The pictures are shown in Figs. 11–13 for EEG, MEG, and EEG/MEG, respectively. The gray tone scale is proportional to \mathcal{V} .

In Figs. 11 and 12, only the points with a volume smaller than 2.10^4 mm^3 are plotted. We see that with EEG alone (Fig. 11), the best accuracy is obtained when the volume of the 90% concentration ellipsoid is of 1660 mm^3 , corresponding to a sphere with a radius of 7.4 mm. This occurs, of course, at points below the EEG cap that are closest to the sphere.

The example of Fig. 12 shows that the MEG achieves a best volume of the 90% concentration ellipsoid of 3710 mm^3 , which corresponds to a sphere with a radius of 9.6 mm. However, it achieves a wider region of reasonable accuracy than EEG. Comparing Figs. 11 and 12, we can also see that the regions of better accuracy are, in a sense, complementary for EEG and MEG.

Notice that the best accuracy in Fig. 13 is obtained at a point somewhere between the region below the EEG cap and where the sphere is closest to the brain surface. This is the point where the synergy between EEG and MEG is at its maximum. The volume \mathcal{V} at these points is 189 mm^3 , which amounts to a sphere of about a 3.6 mm radius. That is, if the precision was the same in all directions, the dipole position would be estimated within a sphere of 3.6 mm with 90% confidence. From Fig. 13, we easily notice how the region of better accuracy has been expanded using EEG and MEG together.

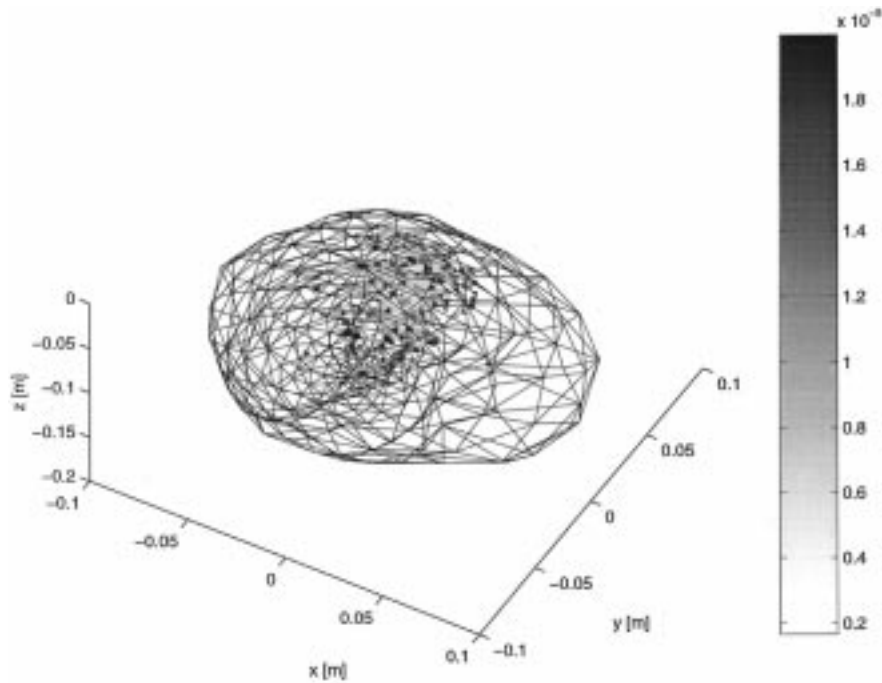


Fig. 11. Volume of 90% probability concentration ellipsoid as a function of dipole location on a spherical surface for EEG. The volume in m^3 is proportional to the tone of gray.

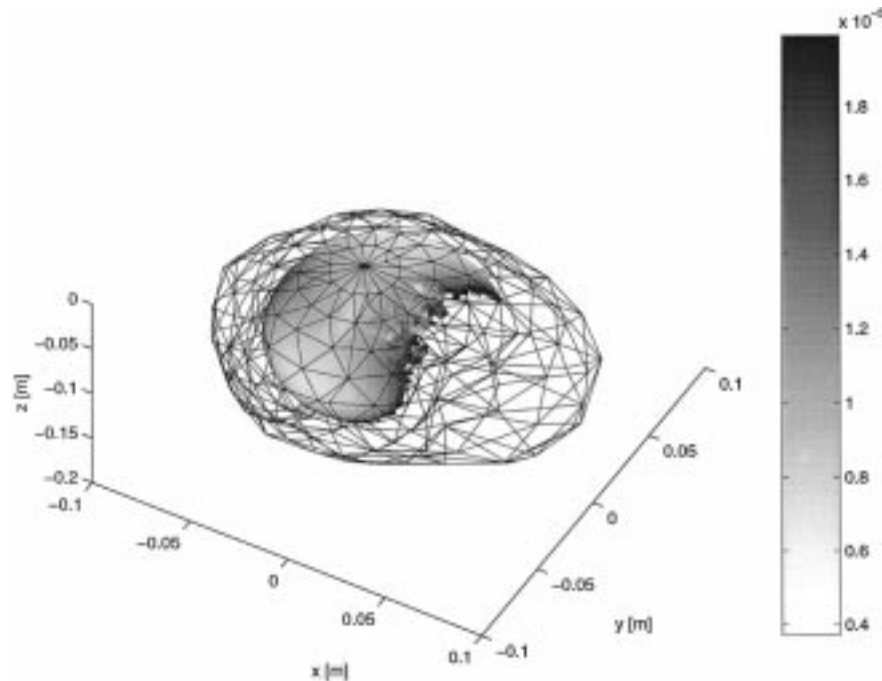


Fig. 12. Volume of 90% probability concentration ellipsoid as a function of dipole location on a spherical surface for MEG. The volume in m^3 is proportional to the tone of gray.

V. DISCUSSION AND CONCLUSIONS

We computed the CRB for estimating the location and moment parameters of a static dipole source of brain activity. Our measurement model is suitable to handle scalar as well as vector sensors taken from an EEG cap, an MEG helmet, or combined EEG/MEG. A realistic head model with layers of different conductivities and arbitrary but known shapes has been assumed.

The relationship between the measurements and the source parameters takes the form of an integral equation. To explicitly obtain this relationship, a solution of the so-called inverse problem would have to be computed. Since this cannot be done analytically in general, we used the BEM or FEM formulation to approximate the required relation. Then, considering the noise model, we computed the bounds. In this way, we introduced a framework that is suitable for computing the CRB for parameter

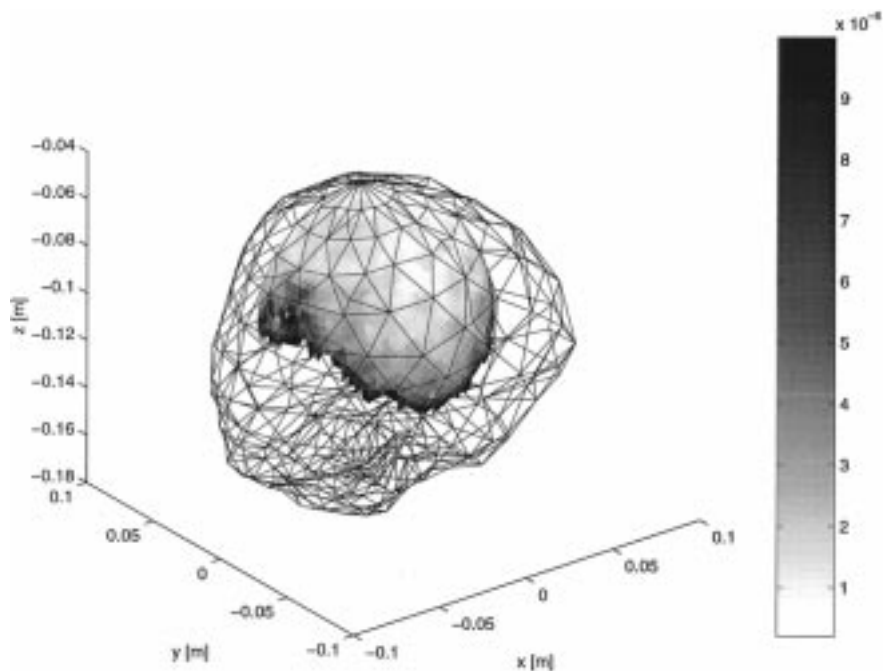


Fig. 13. Volume of 90% probability concentration ellipsoid as a function of dipole location on a spherical surface for EEG/MEG. The volume in m^3 is proportional to the tone of gray.

estimation of a brain source of activity, as well as other similar inverse problems arising in many other areas, as noted in the Introduction.

We illustrated our procedure with examples, using an EEG cap and MEG helmet configuration utilized in [31] and [41] and real head data, as opposed to previous works on bounds where spherical symmetry was assumed. Our examples considered a BEM formulation with constant potential on subdomains and a point collocation technique for the discretization, extending the work of [18], [33], and [34]. The CRB can be utilized in a variety of forms, as we made clear in the Introduction. We presented our numerical example results in different manners. We considered dipoles distributed on a cross-section plane of the brain and obtained contours of equal location accuracy. A second set of examples assumed the dipoles on a spherical surface inside the brain and allowed the presentation of the location and moment accuracy as a function of the dipole position on this surface. Our third example presented the location error bounds that correspond to the three parameters of \mathbf{p} in a concentrated way. Indeed, we depicted the volume of the ellipsoid with 90% probability of enclosing the source of activity for dipoles that are on a spherical surface inside the brain.

The CRB formulation of [18] provided a separation between lateral and depth position error performances for a spherical head model. We adapted these results to our realistic head model and showed its use in the numerical examples. There is a number of issues that influence the performance but have not been studied here, which could be analyzed using the CRB. Examples include the role of the relative position between the EEG cap and the MEG helmet; the number, type and orientation of sensors; and shape and area covered by the arrays.

Among the possible extensions of the present work with a real head is the conditional character of the CRB. Indeed, we have

assumed known conductivities and a precise knowledge of the surfaces separating the head layers. With a Bayesian technique, it would be possible to account for random layer conductivities, following [41]. A description that incorporates the head surface variations among individuals still remains to be found. A deterministic attempt has been presented in [6]. Our approach would allow investigating the effect of head surfaces variability and tessellation errors on estimation accuracy.

ACKNOWLEDGMENT

The authors thank Prof. B. He of The University of Illinois at Chicago for providing data used in the paper and for his helpful comments.

REFERENCES

- [1] A. I. Ahonen, M. S. Hämäläinen, M. J. Kajola, J. E. T. Knuutila, J. T. Simola, and V. A. Vilkmán, "Sampling theory for neuromagnetic detector arrays," *IEEE Trans. Biomed. Eng.*, vol. 40, pp. 859–869, Sept. 1993.
- [2] C. A. Brebbia and J. Domínguez, *Boundary Elements. An Introductory Course*, 2nd ed. New York: McGraw-Hill, 1992.
- [3] K. E. Bullen and B. Bolt, *An Introduction to the Theory of Seismology*. Cambridge, U.K.: Cambridge Univ. Press, 1985.
- [4] R. M. Chapman, R. J. Ilmoniemi, S. Barbanera, and G. L. Romani, "Selective localization of alpha brain activity with neuromagnetic measurements," *Electroencephalogr. Clin. Neurophysiol.*, vol. 58, pp. 569–572, 1984.
- [5] CTF Syst., Inc., "Corporate Website," Port Coquitlam, BC, Canada, <http://www.ctf.com>.
- [6] B. N. Cuffin, "EEG localization accuracy improvements using realistically shaped head models," *IEEE Trans. Biomed. Eng.*, vol. 43, pp. 299–303, Mar. 1996.
- [7] J. C. de Munck, B. W. van Dijk, and H. Spekreijse, "Mathematical dipoles are adequate to describe realistic generators of human brain activity," *IEEE Trans. Biomed. Eng.*, vol. 35, pp. 960–966, Sept. 1988.
- [8] J. C. de Munck, P. C. Vijn, and F. H. Lopes Silva, "A random dipole model for spontaneous brain activity," *IEEE Trans. Biomed. Eng.*, vol. 39, pp. 791–804, Aug. 1992.

- [9] J. C. de Munck, "A linear discretization of the volume conductor boundary integral equation using analytically integrated elements," *IEEE Trans. Biomed. Eng.*, vol. 39, pp. 986–990, Sept. 1992.
- [10] A. Dogandžić and A. Nehorai, "Detecting a dipole source by MEG/EEG and generalized likelihood ratio tests," in *Proc. 30th Asilomar Conf. Signals, Syst. Comput.*, Pacific Grove, CA, Nov. 1996, pp. 1196–1200.
- [11] —, "Estimating evoked dipole responses in unknown spatially correlated noise with EEG/MEG arrays," *IEEE Trans. Signal Processing*, vol. 48, pp. 13–25, Jan. 2000.
- [12] A. S. Ferguson, X. Zhang, and G. Stroink, "A complete linear discretization for calculating the magnetic field using the boundary element method," *IEEE Trans. Biomed. Eng.*, vol. 41, pp. 455–460, May 1994.
- [13] T. Gasser, J. Möcks, and W. Köhler, "Amplitude probability distribution of noise for flash-evoked potentials and robust response estimates," *IEEE Trans. Biomed. Eng.*, vol. BME-33, pp. 579–584, June 1986.
- [14] L. A. Geddes and L. E. Baker, "The specific resistance of biological material, a compendium of data for the biomedical engineer and physiologist," *Med. Biol. Eng.*, no. 5, pp. 271–293, 1967.
- [15] D. B. Geselowitz, "On bioelectric potentials in an inhomogeneous volume conductor," *Biophys. J.*, vol. 7, pp. 1–11, 1967.
- [16] —, "On the magnetic field generated outside an inhomogeneous volume conductor by internal current sources," *IEEE Trans. Magn.*, vol. MAG-6, pp. 346–347, 1970.
- [17] M. S. Hämläinen, R. Hari, R. Ilmoniemi, J. Knuutila, and O. V. Lounasmaa, "Magneto-encephalography—Theory, instrumentation, and applications to noninvasive studies of signal processing of the human brain," *Rev. Mod. Phys.*, vol. 65, pp. 413–497, Apr. 1993.
- [18] B. Hochwald and A. Nehorai, "Magnetoencephalography with diversely oriented and multi component sensors," *IEEE Trans. Biomed. Eng.*, vol. 44, pp. 40–50, Jan. 1997.
- [19] K. H. Huebner, E. A. Thornton, and T. G. Byrom, *The Finite Element Method for Engineers*, 3rd ed. New York: Wiley, 1995.
- [20] R. T. Johnson, W. C. Black, and D. S. Buchanan, "Source detectability for multichannel biomagnetic sensors," in *Proc. Tenth Int. Conf. Biomagn.*, Santa Fe, NM, Feb. 1996.
- [21] L. V. Kantorovich and V. I. Krylov, *Approximate Methods of Higher Analysis*. New York: Interscience, 1958.
- [22] A. Kirsch, *An Introduction to the Mathematical Theory of Inverse Problems*. New York: Springer-Verlag, 1996.
- [23] J. Knuutila and M. S. Hämläinen, "Characterization of brain noise using a high sensitivity 7-channel magnetometer," in *Proc. Biomagn.*, 1988, pp. 186–189.
- [24] C. Kravaris and J. H. Seinfeld, "Identification of parameters in distributed parameter systems by regularization," *SIAM J. Contr. Optim.*, vol. 23, pp. 217–241, 1985.
- [25] B. Lütkenhöner, "Magnetic field arising from current dipoles randomly distributed in a homogeneous spherical volume conductor," *J. Appl. Phys.*, vol. 75, no. 11, pp. 7204–7210, Jun. 1994.
- [26] M. S. Lynn and W. P. Timlake, "The use of multiple deflations in the numerical solution of singular systems of equations with applications to potential theory," *SIAM J. Numer. Anal.*, vol. 5, pp. 303–322, 1968.
- [27] J. Malmivuo and R. Plonsey, *Bioelectromagnetism*. New York: Oxford Univ. Press, 1995.
- [28] J. Malmivuo, V. Suihko, and H. Eskola, "Sensitivity distributions of EEG and MEG measurements," *IEEE Trans. Biomed. Eng.*, vol. 44, pp. 196–208, Mar. 1997.
- [29] J. A. McEwen and G. B. Anderson, "Modeling the stationarity and Gaussianity of spontaneous electroencephalographic activity," *IEEE Trans. Biomed. Eng.*, vol. BME-22, pp. 361–369, Sept. 1975.
- [30] J. C. Mosher, M. E. Spencer, R. M. Leahy, and P. S. Lewis, "Error bounds for MEG and EEG source localization," in *Proc. 26th Asilomar Conf. Signals, Syst., Comput.*, Pacific Grove, CA, Oct. 1992, pp. 150–155.
- [31] —, "Error bounds for MEG and EEG dipole source localization," *Electroencephalogr. Clin. Neurophysiol.*, vol. 86, pp. 303–321, 1993.
- [32] C. H. Muravchik and A. Nehorai, "Localizing and identifying underground objects using gravitational measurements," in *Proc. 28th Asilomar Conf. Signals, Syst., Comput.*, Pacific Grove, CA, Oct. 1994, pp. 760–764.
- [33] —, "MEG/EEG error bounds for a dipole source with a realistic head model," in *Proc. 30th Asilomar Conf. Signals, Syst., Comput.*, Pacific Grove, CA, Nov. 1996, pp. 1386–1390.
- [34] —, "MEG/EEG numerical error bounds for a dipole source with a realistic head model," in *Proc. IEEE Conf. Eng. Med. Biol. Soc.*, Chicago, IL, Oct. 30–Nov. 2, 1997, pp. 1233–1236.
- [35] —, "MEG/EEG error bounds for a dipole source with a realistic head model," Dept. Elect. Eng. Comput. Sci., Univ. Illinois, Chicago, Rep. no. UIC-EECS-99-3, May 1999.
- [36] C. H. Muravchik, O. N. Bria, and A. Nehorai, "E/MEG error bounds for a dynamic dipole source with a realistic head model," *Meth. Inform. Med.*, vol. 39, no. 2, pp. 110–114, June 2000.
- [37] Neuromag Ltd., Helsinki, Finland, <http://www.neuromag.com/main.html>.
- [38] R. D. Pascual-Marqui and R. Biscay-Lirio, "Spatial resolution of neuronal generators based on EEG and MEG measurements," *Int. J. Neurosci.*, vol. 68, pp. 93–105, 1993.
- [39] M. E. Pflieger, G. V. Simpson, S. P. Ahlfors, and R. J. Ilmoniemi, "Superadditive information from simultaneous MEG/EEG data," in *Proc. Tenth Int. Conf. Biomagn.*, Santa Fe, NM, Feb. 1996.
- [40] B. Porat, *Digital Processing of Random Signals: Theory and Methods*. Englewood Cliffs, NJ: Prentice-Hall, 1994.
- [41] B. M. Radich and K. M. Buckley, "EEG dipole localization bounds and MAP algorithms for head models with parameter uncertainties," *IEEE Trans. Signal Processing*, vol. 42, pp. 233–241, Mar. 1995.
- [42] G. R. Richter, "An inverse problem for the steady state diffusion equation," *SIAM J. Appl. Math.*, vol. 41, pp. 210–221, 1981.
- [43] D. S. Ruchkin, "An analysis of average response computations based upon aperiodic stimuli," *IEEE Trans. Biomed. Eng.*, vol. BME-12, pp. 87–94, 1965.
- [44] S. Rush and D. A. Driscoll, "Current distribution in the brain from surface electrodes," *Anest. Analg.*, vol. 47, pp. 717–723, 1968.
- [45] H. Schlitt, L. Heller, R. Aaron, E. Best, and D. Ranken, "Evaluation of boundary element methods for the EEG forward problem: Effect of linear interpolation," *IEEE Trans. Biomed. Eng.*, vol. 42, pp. 52–58, Jan. 1995.
- [46] D. J. Staton, S. H. Allos, L. A. Bradshaw, W. O. Richards, and J. P. Wikswo, "Noninvasive measurement of the vector magnetic field from human gastrointestinal sources," in *Proc. Tenth Int. Conf. Biomagn.*, Santa Fe, NM, Feb. 1996.
- [47] V. L. Towle, L. Khorasani, E. M. Berkson, I. Syed, C. H. Pelizzari, D. Jewett, and J.-P. Spire, "Human somatosensory evoked potential dipoles: How accurate are the localizations," in *Proc. IEEE Conf. Eng. Med. Biol. Soc.*, Chicago, IL, Oct. 30–Nov. 2, 1997, pp. 2616–2621.
- [48] Y. Uchikawa, K. Kobayashi, K. Sakawa, and M. Kotani, "Separation of overlapping sources induced by the mixed stimulations using 3-dimensional MEG mappings," in *Proc. Tenth Int. Conf. Biomagn.*, Santa Fe, NM, Feb. 1996.
- [49] H. L. Van Trees, *Detection, Estimation and Modulation Theory*. New York: Wiley, 1968, pt. I.
- [50] S. van den Broek, H. Zhou, and M. J. Peters, "Computation of neuro-magnetic fields using finite-element method and biot-savart law," *Med. Biol. Eng. Comput.*, vol. 34, pp. 21–26, Jan. 1996.
- [51] J. Vrba, V. Angus, K. Betts, M. B. Burbank, and T. Cheung *et al.*, "143 channel whole-cortex MEG system," in *Proc. Tenth Int. Conf. Biomagn.*, Santa Fe, NM, Feb. 1996.
- [52] Y. Yoshida, A. Arakawa, Y. Kondo, S. Kajihara, S. Tomita, T. Tomita, N. Matsuda, and Y. Takanashi, "A 129-channel vector neuromagnetic imaging system," in *Proc. Tenth Int. Conf. Biomagn.*, Santa Fe, NM, Feb. 1996.



Carlos H. Muravchik (S'81–M'83–SM'99) was born in Argentina on June 11, 1951. He received the B.Sc. degree in electronics engineering from the Universidad Nacional de La Plata, La Plata, Argentina, in 1973 and the M.Sc. degree in statistics and the Ph.D. degree in electrical engineering from Stanford University, Stanford, CA, in 1980 and 1983, respectively.

He is currently a Professor with the Department of Electrical Engineering, Universidad Nacional de La Plata and a member of its Industrial Electronics, Control, and Instrumentation Laboratory (LEICI). He is also a member of the Comisión de Investigaciones Científicas de la Provincia de Buenos Aires. He was a Visiting Professor at Yale University, New Haven, CT, in 1983 and 1994 and at the University of Illinois at Chicago in 1996, 1997, and 1999. His research interests are in the area of statistical signal and array processing with biomedical, control and communications applications, and nonlinear control systems.



Arye Nehorai (S'80–M'83–SM'90–F'94) received the B.Sc. and M.Sc. degrees in electrical engineering from the Technion—Israel Institute of Technology, Haifa, in 1976 and 1979 respectively, and the Ph.D. degree in electrical engineering from Stanford University, Stanford, CA, in 1983.

After graduation, he worked as a Research Engineer for Systems Control Technology, Inc., Palo Alto, CA. From 1985 to 1995, he was with the Department of Electrical Engineering, Yale University, New Haven, CT, where he became an Associate Professor in 1989. In 1995, he joined the Department of Electrical Engineering and Computer Science, The University of Illinois at Chicago (UIC) as a Full Professor. He is currently Chair of the Department's Electrical and Computer Engineering Division and is managing the creation of a new ECE Department at UIC. He holds a joint professorship with the Bioengineering Department at UIC. His research interests are in signal processing, communications, and biomedicine. He is an Associate Editor of *Circuits, Systems, and Signal Processing* and *The Journal of the Franklin Institute* and a Member of the Editorial Board of *Signal Processing*.

Dr. Nehorai is currently the Editor-in-Chief of the IEEE TRANSACTIONS ON SIGNAL PROCESSING. He is also a Member of the Publications Board of the IEEE Signal Processing Society. He has previously been an Associate Editor of the IEEE TRANSACTIONS ON ACOUSTICS, SPEECH, AND SIGNAL PROCESSING, of IEEE SIGNAL PROCESSING LETTERS, the IEEE TRANSACTIONS ON ANTENNAS AND PROPAGATION, and the IEEE JOURNAL OF OCEANIC ENGINEERING. He served as Chairman of the Connecticut IEEE Signal Processing Chapter from 1986 to 1995 and is currently the Chair and a Founding Member of the IEEE Signal Processing Society's Technical Committee on Sensor Array and Multichannel (SAM) Processing. He was the co-General Chair of the First IEEE SAM Signal Processing Workshop, which was held in 2000. For the year 1979/1980, he received the Rothschild Fellowship in science and engineering, which is awarded annually to eight new graduates throughout Israel. He was co-recipient, with P. Stoica, of the 1989 IEEE Signal Processing Society's Senior Award for Best Paper. He received the Faculty Research Award from UIC College of Engineering in 1999. He has been a Fellow of the Royal Statistical Society since 1996.

Dr. Nehorai is currently the Editor-in-Chief of the IEEE TRANSACTIONS ON SIGNAL PROCESSING. He is also a Member of the Publications Board of the IEEE Signal Processing Society. He has previously been an Associate Editor of the IEEE TRANSACTIONS ON ACOUSTICS, SPEECH, AND SIGNAL PROCESSING, of IEEE SIGNAL PROCESSING LETTERS, the IEEE TRANSACTIONS ON ANTENNAS AND PROPAGATION, and the IEEE JOURNAL OF OCEANIC ENGINEERING. He served as Chairman of the Connecticut IEEE Signal Processing Chapter from 1986 to 1995 and is currently the Chair and a Founding Member of the IEEE Signal Processing Society's Technical Committee on Sensor Array and Multichannel (SAM) Processing. He was the co-General Chair of the First IEEE SAM Signal Processing Workshop, which was held in 2000. For the year 1979/1980, he received the Rothschild Fellowship in science and engineering, which is awarded annually to eight new graduates throughout Israel. He was co-recipient, with P. Stoica, of the 1989 IEEE Signal Processing Society's Senior Award for Best Paper. He received the Faculty Research Award from UIC College of Engineering in 1999. He has been a Fellow of the Royal Statistical Society since 1996.